

CIPS PMC Level 2 Data: Orbit-by-Orbit Cloud Parameters

Last Updated January 2023

1. Introduction

CIPS PMC version 4.20 Level 2 data files consist of measurements of cloud parameters on an orbit-by-orbit basis. These files are provided for quantitative analyses of the CIPS retrievals at high spatial resolution. For those users interested mainly in averaged quantities, the CIPS team also provides level 3C “summary” files – these are files that contain one PMC season each of orbit-by-orbit quantities binned in 1-degree latitude bins (separate binning for ascending and descending node data). More information can be found in the level 3C documentation.

For details of the retrieval, readers are referred to the CIPS algorithm paper [Lumpe *et al.*, 2013], which can be found at <http://dx.doi.org/10.1016/j.jastp.2013.06.007>. In this document we describe the CIPS PMC level 2 data products and provide guidance for data users. The scientific validity of the CIPS data has been established through its use in a variety of scientific and validation analyses. The CIPS cloud frequencies and albedo have been found to agree very well with coincident measurements from the Solar Back Scatter Ultraviolet (SBUV-2) instruments [Benze *et al.*, 2009; 2011], and are considered valid for scientific analysis with the caveats described below. Baumgarten *et al.* [2012] have analyzed CIPS data obtained in close coincidence with ground-based lidar measurements and found good agreement in the cloud brightness observed by these two very different methods. The detailed spatial structures observed by CIPS have been used to study mesospheric gravity waves [Chandran *et al.*, 2009; 2010, 2012] and planetary waves [Merkel *et al.* 2009], while the CIPS ice water content has been used by Stevens *et al.* [2010] to analyze the effect of tidal signatures on PMC. CIPS cloud frequencies were used in Karlsson *et al.* [2011] to connect SH PMC variability with the breakdown of the wintertime SH stratospheric polar vortex. The SH intra-seasonal PMC variability observed by CIPS was also used to investigate inter-hemispheric coupling in Karlsson *et al.* [2009]. Stevens *et al.* [2012] used the CIPS observations of PMC frequency and albedo in July 2011 to help demonstrate a causal link between the occurrence of very bright clouds and the main engine exhaust from the space shuttle’s final flight.

At the current time, three NetCDF data files and three png image files are available for each orbit. These data files are:

- (1) Geolocation, including variables such as latitude, longitude, time, etc. The file name extension is _cat.nc.
- (2) Cloud properties, including albedo, particle radius, and ice water content. The file name extension is _cld.nc.
- (3) Cloud phase function, containing cloud albedo vs. scattering angle. The file name extension is _psf.nc.
- (4) Orbit-strip image of cloud albedo. The file name extension is _alb.png.
- (5) Orbit-strip image of particle radius. The file name extension is _rad.png.

(6) Orbit-strip image of ice water content. The file name extension is `_iwc.png`.

Variables in files (1) through (3) are described in tables at the end of this document. There are ~15 orbits per day. Each orbit contains 27 images in each camera (30 for the PX camera) and covers about 8000 km along the orbit and about 900 km in the cross-track direction. Cloud properties and associated geolocation variables are provided with 25-km² resolution along the orbit track; resolution elements are 5 km × 5 km in the nadir, and become elongated away from nadir (but remain 25 km² in total area covered).

Data arrays in the level 2 files provide cloud properties in each 25-km² resolution element (hereafter referred to as a level 2 “pixel”), with array dimensions corresponding to the number of elements in the along-track and cross-track directions. Each array element thus corresponds to a unique location (latitude and longitude) that is observed up to ten times with different observation geometries, and thus scattering angles (see Lumpe et al. [2013] for a description of the viewing geometry and measurement approach). For convenience in data handling, the arrays span the entire bounding box defined by a CIPS orbit, consisting of ~800,000 elements. However roughly half of these elements correspond to locations where no measurements are made and therefore have fill values.

The compressed geolocation, cloud property and phase function NetCDF files are ~5, 1, and 25 MB in size, respectively. Uncompressed file sizes are much larger due to the significant fraction of fill (NaN) values in these files (see below). Most users of level 2 data will not need the cloud phase function file; it is provided mainly for users who wish to re-derive such parameters as cloud particle radius using independent algorithms.

Documentation and IDL software tools to read the level 2 NetCDF files are available for download from the AIM web site. NetCDF readers for other software packages are available elsewhere (see, for instance, <http://www.unidata.ucar.edu/software/netcdf/software.html>).

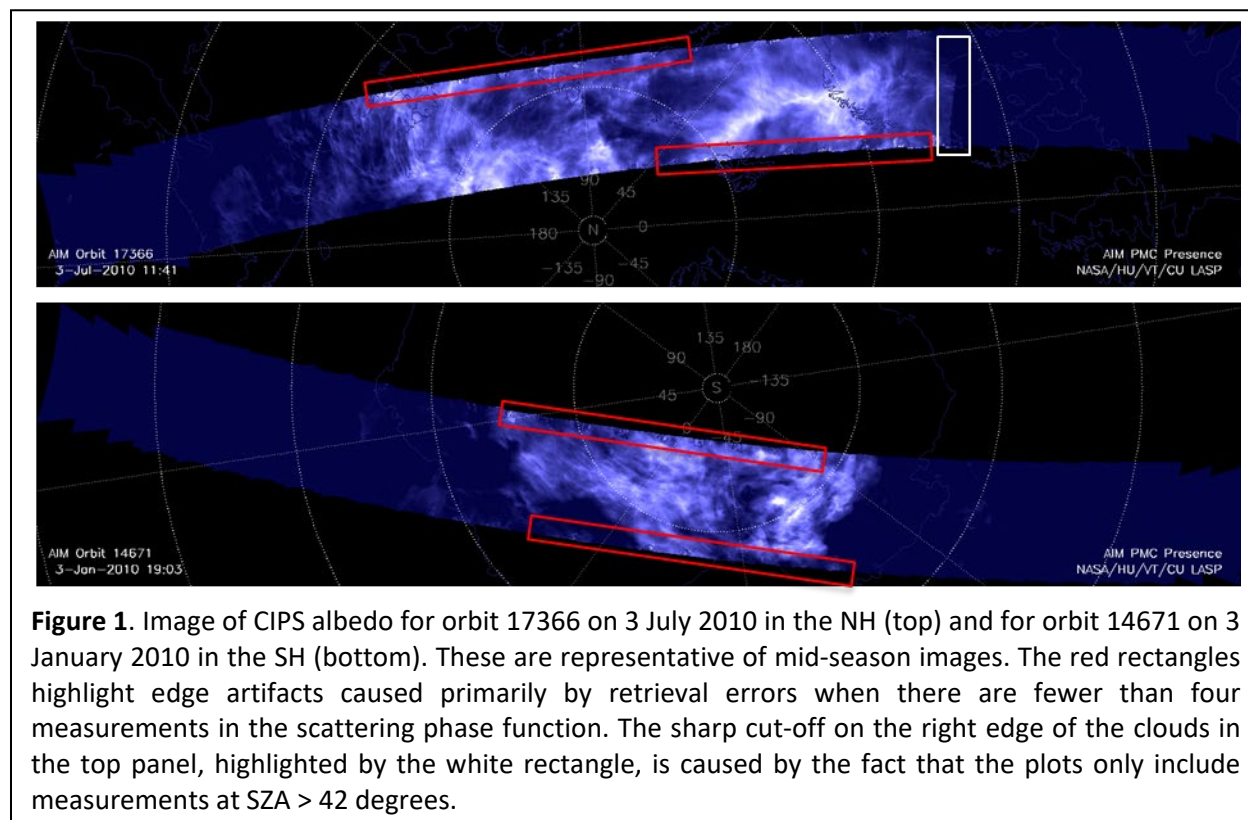
The CIPS level 2 retrievals are performed over a solar zenith angle (SZA) range from 40 to 95 degrees on each orbit [Lumpe *et al.*, 2013]. The range of scattering and view angles observed for each location changes along the orbit track, but always includes 90° scattering angle. For uniformity and comparison to other data sets, the cloud albedo reported in files (2) and (4) is therefore normalized to 90° scattering angle and nadir (0°) view angle. The view angle correction is accomplished by removing the $\sec(\theta)$ geometry factor to account for the view angle dependence in path length (where θ , the view angle, is the angle between the satellite and zenith directions, as measured from the scattering volume). The scattering angle correction is accomplished by obtaining the best fit of the observed phase function (albedo vs. scattering angle) to a set of assumed scattering phase functions that are constrained by lidar data (for a comprehensive discussion see Lumpe *et al.* [2013]; also see Hervig *et al.* [2009] and Baumgarten *et al.* [2010]). Here we make the assumptions that the ice particles have an axial ratio of 2 and a distribution width that varies approximately as $0.39 \times \text{radius}$ for radii up to 40 nm and then stays

fixed at ~ 15.8 nm for larger particles. The albedo at 90° scattering angle from that best fit is the value to which the view angle correction is applied.

2. Orbit Strip Images

Users interested in a quick, qualitative view of the data for a particular orbit should download the albedo image png files (type (4) in the list above). These images omit all data with $\text{SZA} < 42^\circ$, since the Rayleigh background subtraction is prone to higher errors at these angles. In defining the color scale for each image, the plotting routine imposes a limit on the albedo of $2 \times 10^{-6} \text{ sr}^{-1}$ as a lower threshold for plotting; thus any clouds dimmer than this will not appear. The upper plotting threshold is set so that 0.1% of the pixels are saturated, unless this threshold is less than 10^{-5} sr^{-1} . In that case, the threshold is set to equal 10^{-5} sr^{-1} . Since color scales for these png files are determined uniquely for each orbit, these images should not be used to compare cloud brightness from one orbit to the next. For that purpose, users should download the NetCDF files. The particle radius and ice water content images – types (5) and (6) above – are made using the identical data screening used for the albedo images.

Figure 1 shows examples of orbit strip albedo images for both the northern hemisphere (NH) and southern hemisphere (SH). (Note that the sample data shown in this document is from the V4.20 revision 04 data; however the latest revision 05 release looks identical). These measurements were made on 3 July 2010 and 3 January 2010, respectively, and are representative of CIPS observations in the middle of the PMC season. Latitude lines are drawn in ten-degree increments from 80° to the lowest latitude observed. Note that images in the NH curve downward, whereas images in the SH curve upward. Each orbit strip nominally consists of overlapping measurements

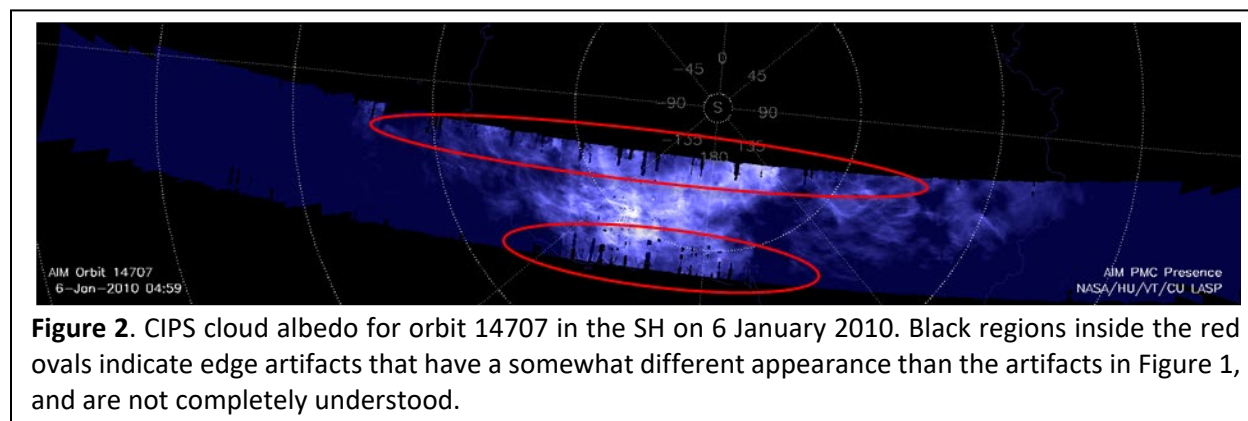


from 27 different 4-camera scenes. The scene-to-scene transitions are essentially seamless in the v4.20-processed data, a substantial improvement over past versions of the CIPS data resulting from the improved background subtraction algorithm in v4.20. As can be seen from these two examples, the CIPS images contain a wealth of information on the cloud structures, which can be analyzed quantitatively using the level 2 NetCDF files.

The remainder of this section describes some anomalies of which users should be aware in the albedo png file images. Many of these are simply results of the observing geometry, but others are caused by retrieval artifacts. If images are found to exhibit suspicious behavior that is not described here, we would very much appreciate being informed (please send an email to aimsds@lasp.colorado.edu).

2.1. Edge Artifacts

The retrieval algorithm relies on multiple observations of the same location, with different scattering angles. Throughout most of the orbit, each location is observed at 6 or more different scattering angles, allowing for a robust measurement of the scattering phase function. At the cross-track edges of the orbit, however, fewer measurements are made of a single location. This often leads to errors in the retrievals, resulting in the "railroad track" or "film sprocket" pattern that is highlighted by the red rectangles in Figure 1. On occasion, these edge artifacts take on a different appearance, as shown in Figure 2 (indicated by the red ovals). We are still working to diagnose causes for the different characteristics of these artifacts.



In the v4.20 NetCDF data files, the level 2 quality flag indicates the number of scattering angles in the phase function. A quality flag of 0 means six or more measurements; 1 means four or five measurements, and 2 means three or fewer measurements. Because of artifacts such as shown here, caution is particularly warranted when the quality flag is 2. Since the particle radius and ice water content (which is derived from the radius) are in particular adversely affected by an underdetermined phase function, these quantities are not retrieved for pixels with quality flag 2 and default values (-999) are entered in the level 2 NetCDF files.

2.2. Solar Zenith Angle Screening

The level 2 png files apply a screening for SZA: Measurements are only included for $42^\circ < \text{SZA}$. Figure 1 shows the effect of not including any data in the images for $\text{SZA} < 42^\circ$. This results in the

hard cutoff on the right-hand side of the NH image (descending node data). Although this feature is not obvious in the SH image in Figure 1, it does occur in the SH (but on the left-hand side (ascending node) of the images). Note that the NetCDF files include all data; they are not screened for SZA. The SZA values are included in the NetCDF files, however, and we recommend caution if the SZA is less than 42° . The reasons for this are described in section II.

2.3. Rolled Images

Starting in the SH 2007-2008 season and continuing through the SH 2009-2010 season, the AIM satellite rolled to one side during images taken near the common volume ($\sim 90^\circ$ SZA), in order to place the SOFIE line of sight within the CIPS field of view. The amount of roll depends on the satellite beta angle, which changes with time. This can lead to unusual geometries of the cameras, an example of which is given in Figure 3. The change in the orientation of the orbit strip is indicated by the red oval in this figure, showing that the roll causes the field of view to become somewhat elongated at the camera edges. The data corresponding to large roll angles can have very high satellite view angles. Because these measurements are known to have higher than normal systematic errors in the background Rayleigh subtraction, the CIPS retrievals require at least one measurement in the scattering phase function to have a view angle of less than 60° . This criterion is often not satisfied in parts of the rolled region, which explains the lack of clouds at the edge of the rolled area. It also gives rise to the sharp, zig-zag edges in the clouds highlighted by the red oval – this zig-zag pattern denotes the boundary beyond which view angles are all larger than 60° .

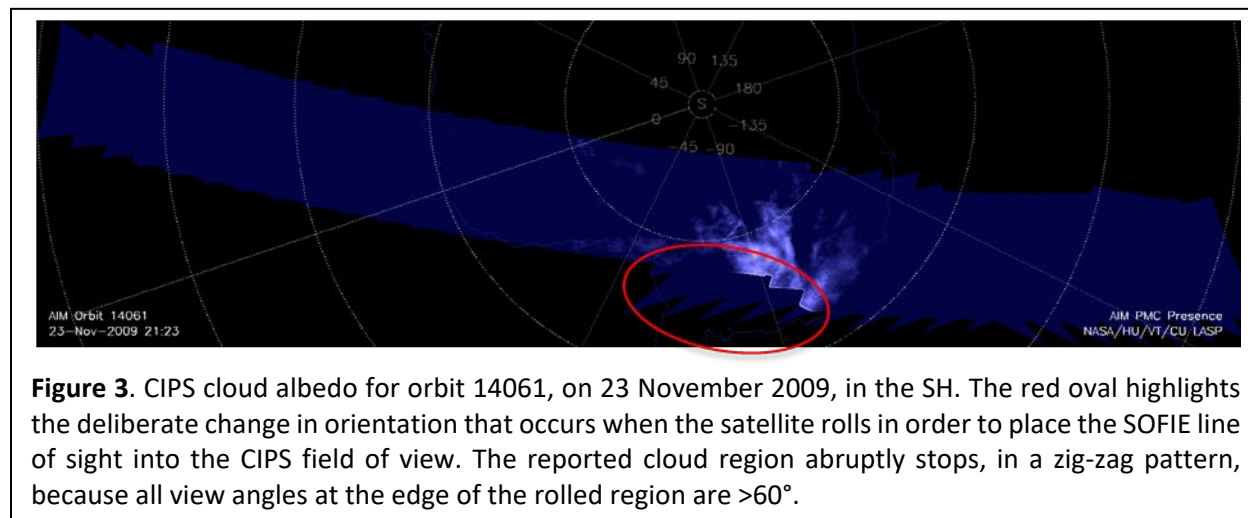
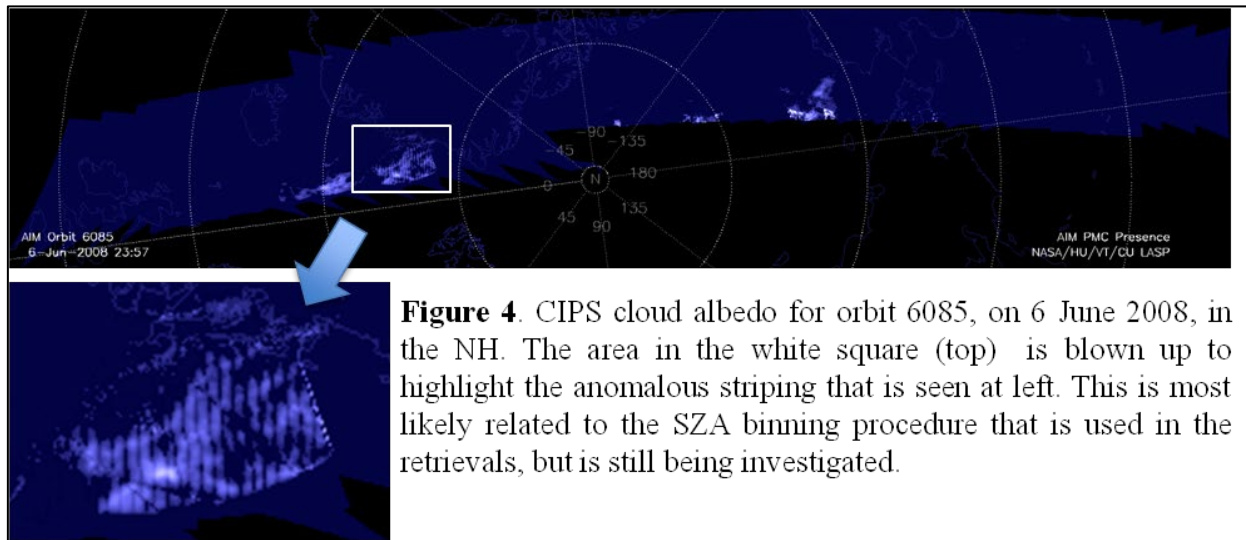


Figure 3. CIPS cloud albedo for orbit 14061, on 23 November 2009, in the SH. The red oval highlights the deliberate change in orientation that occurs when the satellite rolls in order to place the SOFIE line of sight into the CIPS field of view. The reported cloud region abruptly stops, in a zig-zag pattern, because all view angles at the edge of the rolled region are $>60^\circ$.

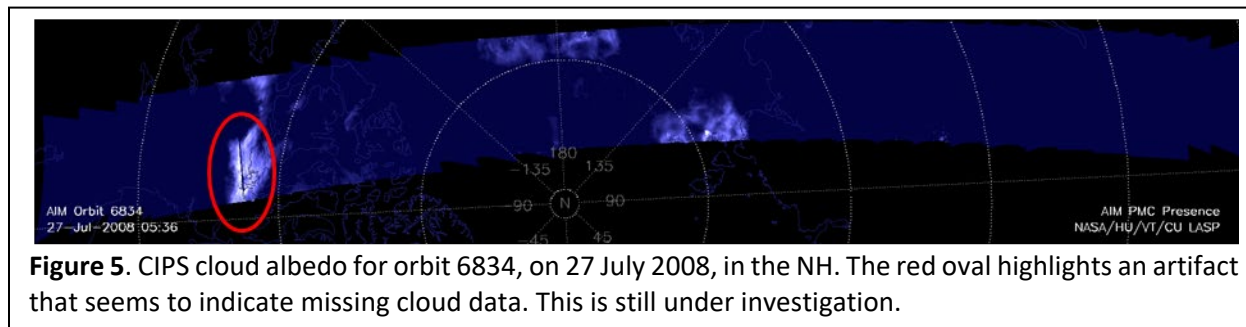
2.4. Striping Near Edge of Orbit Strips

On occasion, clouds will exhibit a type of "striping" pattern (see Figure 4), which looks somewhat like signals that might be expected from the presence of gravity waves. However, these patterns always occur near the edge of the orbit strip, are oriented in the cross-track direction, and have a much more regular appearance than expected from a real geophysical phenomenon. We are still investigating the cause of these patterns. It is likely that the stripes are artifacts that arise from some combination of sampling (e.g., fewer points in the phase function near the edges of the orbit strips), and the fact that the retrievals use a 0.25° SZA grid.



2.5. Blank stripe near 90° SZA

Figure 5 shows an example of an artifact that on rare occasions appears near the high-SZA edge of the orbit strips. This artifact manifests itself as an area of apparently missing cloud data. The problem is that the retrieved ozone column, which is needed to calculate the Rayleigh scattering background, goes negative; thus the Rayleigh background becomes undefined, which means no clouds are detected. It appears as a stripe because it only occurs for one or a few SZA bins. The root cause of this is still under investigation and will be fixed in version 5.

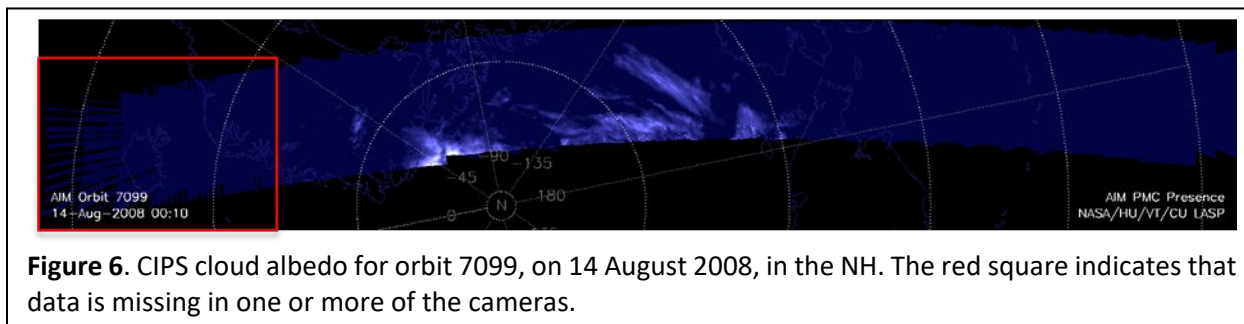


2.6. Missing Data

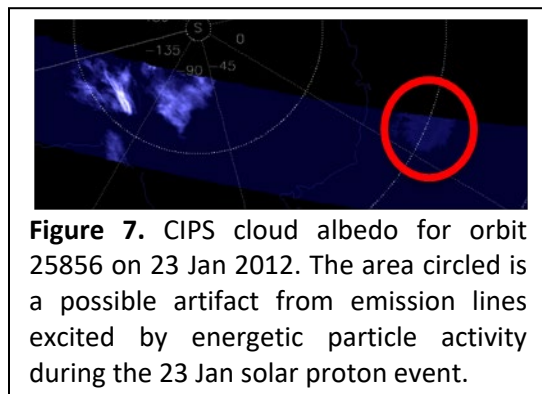
Figure 6 gives an example of what an orbit strip looks like when data is missing from one or more cameras. This happens only rarely, and the cause is still under investigation. On occasion, data is missing from all cameras for part of an orbit. In this case, an orbit strip is plotted, but only over the spatial region for which data is obtained. An example of this is orbit 25012, on 27 Nov 2011 (not shown).

2.7. High Geomagnetic Activity

Figure 7 shows a possible artifact from the solar proton event that began on 23 January 2012. Under conditions of high geomagnetic activity, transitions in the N_2 and NO molecules can be



excited by energetic particles (protons and/or electrons) – as these molecules fall back to their ground state, they emit radiation in the CIPS wavelength band near 265 nm. Thus it is possible for CIPS to mistakenly identify these emissions as cloud scattering. More analysis is required before we can definitively state that this is occurring, but we urge caution when interpreting images during or shortly after times of high geomagnetic activity.



3. Guidance for NetCDF files

The NetCDF files listed in section 1 enable users to quantitatively analyze the data plotted in the orbit strip images. Here we provide guidance for using file types (1) and (2), emphasizing data limitations of which users should be aware. Users interested in the phase function files are encouraged to contact us directly (aimsds@lasp.colorado.edu) for guidance with these files.

Many of the potential artifacts were mentioned in section II, but will be described in this section as well. In addition, in this section we point out other features in the data that we believe do not yet warrant scientific analysis. Some general guidelines are summarized in at the end of this document. Because there will be exceptions to these guidelines, we encourage users to contact us (aimsds@lasp.colorado.edu) with any questions or concerns.

3.1. Quality Flags

The v4.20 quality flags (QF) are very rudimentary at this point. In the future, they will contain information about estimated errors. At the current time, however, they are based only on the number of measurements in the scattering phase function at each geographic location, from which the cloud albedo, particle radius, and ice water content are derived.

As explained in the algorithm description document, retrieval of the cloud properties relies first on distinguishing the cloud particle scattering phase function from the Rayleigh background scattering phase function, and then on characterizing the particle radius by matching the retrieved phase function to one of a set of phase functions derived empirically from lidar observations. When the scattering phase function is defined by six or more measurements at different scattering angles, the retrievals are robust, and are assigned QF=0. Larger uncertainties

are inherent in retrievals with measurements at fewer scattering angles. $QF=1$ corresponds to four or five measurements at different scattering angles, and $QF=2$ corresponds to three or fewer measurements at different scattering angles. Particle radius and ice water content are not reported for $QF > 1$; caution is warranted when interpreting albedo values for $QF > 1$.

Figures 8 and 9 give examples of the locations of measurements with different QF values. These figures show the latitude/longitude of all measurements on arbitrary orbits in the NH on 21 June (Figure 8) and in the SH on 21 December (Figure 9) in different years. As explained more in the next section, we do not recommend using v4.20 data for $SZA < 42^\circ$ (or $> 95^\circ$, which are already excluded in the level 2 algorithm); these locations are indicated by the gray points. The QF values are indicated by the colors on the ascending/descending nodes as follows: red/purple ($QF=0$); yellow/blue ($QF=1$); green/cyan ($QF=2$). The majority of the locations correspond to $QF=0$, or more than 5 measurements of the

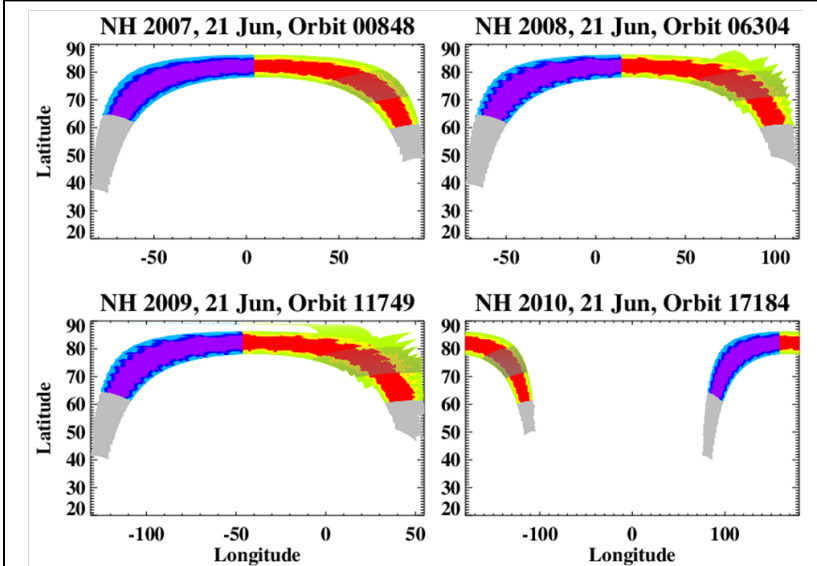


Figure 8. Locations of CIPS measurements in the NH for arbitrary orbits on 21 June in 2007 (top left), 2008 (top right), 2009 (bottom left), and 2010 (bottom right). Gray points indicate $SZA < 42^\circ$ or $SZA > 95^\circ$. Ascending node data are plotted in red/yellow/green, with descending node data in cyan/blue/purple. Purple/Red points correspond to $QF=0$, blue/yellow to $QF=1$, and cyan/green to $QF=2$. The shaded area on the ascending node denotes $75^\circ < SZA < 85^\circ$.

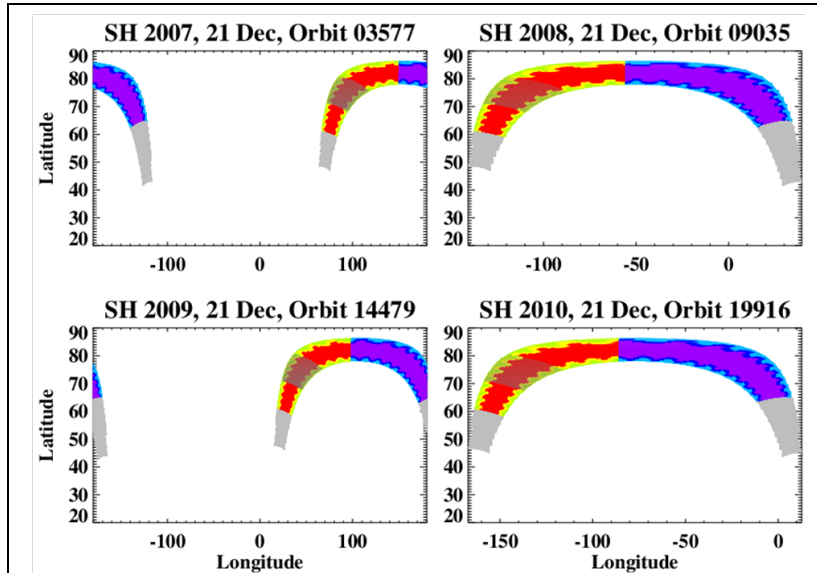


Figure 9. Same as Figure 8, but for arbitrary SH orbits on 21 December.

same location at different scattering angles. Locations at the cross-track edges of the orbits correspond to the higher QF values (less robust retrievals). Also noticeable in Figure 8 is the distorted geometry caused by the spacecraft roll to align CIPS with the SOFIE measurement locations (e.g., orbits 6304 and 11749); this was mentioned above in the description of Figure 3.

Finally, the shaded area on the ascending node in each of the orbits in Figures 8 and 9 corresponds to measurements with $75^\circ < \text{SZA} < 85^\circ$, the significance of which is discussed below.

3.2. Solar Zenith Angle Screening

As noted above, we recommend caution if the solar zenith angle (SZA) is less than 42° (gray points in Figures 8 and 9). This restriction is related to our ability to adequately define the scattering phase function. Ideally, the measurements of a single location would include six or more observations ($\text{QF}=0$), covering a wide range of scattering angles. The geometry of the

CIPS observations dictates, however, that the range of scattering angles sampled at any given SZA decreases with decreasing SZA (see Figure 10). At high SZA, CIPS samples more forward scattering (scattering angles less than 90°). For typical PMC particle sizes, forward scattering is stronger than backward scattering, so signals are largest at small scattering angles, all other things being equal. This, combined with the fact that background Rayleigh scattering decreases at high SZA, enhances the discrimination between cloud and background contributions in the measured scattering phase function, and hence increases the detection sensitivity at high SZAs.

Figure 11 shows the estimated CIPS cloud detection sensitivity vs. cloud albedo and SZA from Lumpe *et al.* [2013]. Note that this is only an example for one particular orbit, but it serves to illustrate the issue. We define a standard CIPS albedo unit as $1 \text{ "G"} = 10^{-6} \text{ sr}^{-1}$. The figure can be interpreted to mean that, e.g., the dimmest (2G)

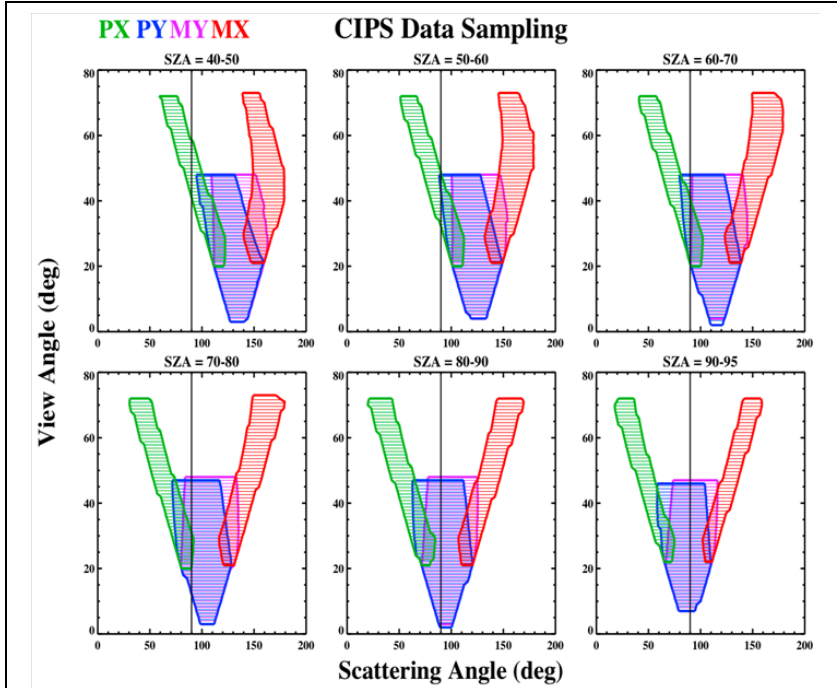


Figure 10. This figure illustrates the typical range of view angle and scattering angle sampled by each CIPS camera, and their dependence on solar zenith angle. Each panel corresponds to a different solar zenith angle bin, ranging from 40 to 95 degrees. This sampling pattern is the same in both hemispheres. From Lumpe *et al.* [2013].

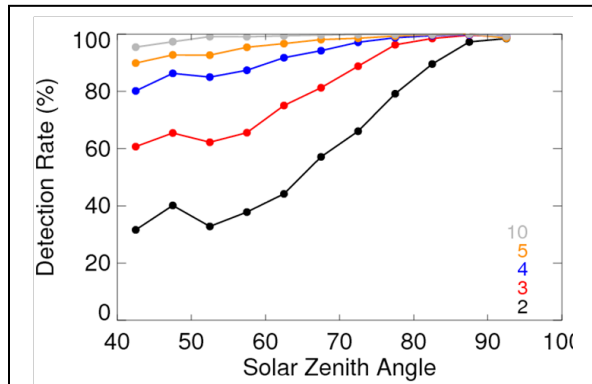


Figure 11. CIPS cloud detection sensitivity derived from simulated retrievals. The five curves correspond to different cloud albedo values, as denoted by the legend (in standard albedo units of 10^{-6} sr^{-1}). The cloud detection rate (in %) is defined as the fraction of clouds of that brightness detected at a given solar zenith angle. From Lumpe *et al.* [2013].

clouds are detected only ~30% of the time at the lowest SZA, whereas the detection rate rises to 60% by 70 degrees SZA and is essentially 100% at the terminator (90 degrees). The detection sensitivity increases rapidly with cloud brightness, so that 5G and brighter clouds are detected with greater than 90% accuracy at all SZA. Further work is underway to improve our retrievals at lower SZAs. The CIPS team recommends using an albedo threshold of 1-2G as an effective way to screen out false detections in CIPS level 2 data.

As discussed more below and in Lumpe *et al.* [2013], the CIPS retrievals show an increase in false detections at SZAs near 80° which is thought to be related to artifacts in the Rayleigh background removal. Users should therefore be cautious when investigating dim clouds for locations corresponding to SZA near 80°.

3.4. Albedo Threshold

The accuracy with which a cloud is detected, and with which the properties of albedo, particle size, and ice water content (IWC) are determined, naturally depends on the cloud albedo, since this dictates the amount of light scattered to the detector. Figure 12 compares cloud parameters that are obtained for the NH 2010 season when averaging over only those measurements for which the albedo is larger than $1 \times 10^{-6} \text{ sr}^{-1}$ (left), $2 \times 10^{-6} \text{ sr}^{-1}$ (middle), or $5 \times 10^{-6} \text{ sr}^{-1}$ (right). Note that with our definition of the unit "G", these thresholds are equivalent to 1G, 2G, and 5G. The advantage of using lower thresholds is that more (total) clouds are detected. The advantage of using higher thresholds is that fewer false detections are included. The plots in Figure 12 were made with the level 3C "summary" files, for which the data were binned into 1-degree latitude bins (see the level 3C documentation). In addition, level 3C data omit all measurements with $\text{SZA} < 42^\circ$ or $\text{SZA} > 94^\circ$, with $\text{QF}=2$, and with radius $\leq 20 \text{ nm}$ (note – as of the last update to this document the NH 2013 season data has implemented a more restrictive high-SZA cutoff of 92 degrees to eliminate the effects due to a transient PX camera artifact. See online documentation.). Recall also that if $\text{QF}=2$, no radius or IWC data are reported in the level 2 files, so by definition the level 3C files will also not contain these data. The Figure 12 plots of albedo, radius, and IWC show values only for cloud points (`cloud_presence_map = 1`; see Table 2 below); they do not average in non-cloud data. Data were binned separately for the ascending and descending nodes, and Figure 12 presents results for the ascending node. Descending node results are qualitatively similar, except as discussed below.

The frequency data in Figure 12 have a clearly defined low-latitude cut-off. This is caused by the level 3C SZA screening. Data at lower latitudes than the cut-off on the ascending node all correspond to $\text{SZA} > 94^\circ$; this is a slightly conservative cut-off, as we believe the data are reliable out to $\text{SZA}=95^\circ$, as noted above. Data at lower latitudes than the cut-off on the descending node all correspond to $\text{SZA} < 42^\circ$. Less conservative analysis of the data yields, as expected, more data at the lower latitudes, but with higher uncertainty. See Figures 8 and 9 for single-orbit (level 2 data) examples of the latitudes corresponding to SZA-screened data. As an aside, the CIPS team has developed a cloud detection algorithm that is similar to that applied to the Solar Backscatter Ultraviolet measurements, which performs better at low SZA. This product is currently being developed for release with the next CIPS data version; see Benze *et al.* [2009; 2011] for a description of the method.

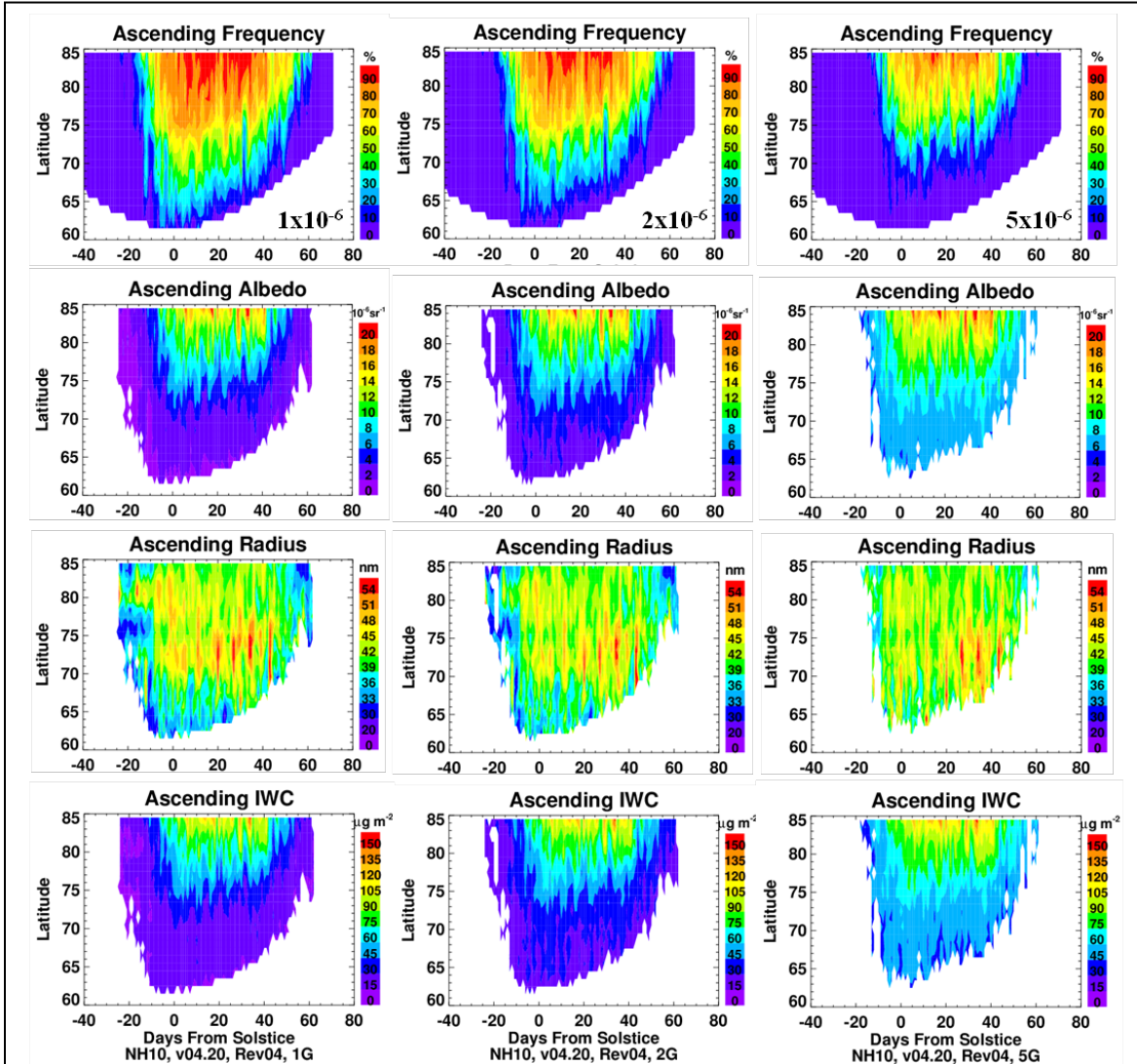


Figure 12. CIPS ascending node PMC frequencies (top), albedo (row 2), radius (row 3), and IWC (bottom) for the NH 2010 season. The columns show the results for measurements that include only those clouds brighter than $1 \times 10^{-6} \text{ sr}^{-1}$ (left), $2 \times 10^{-6} \text{ sr}^{-1}$ (middle) and $5 \times 10^{-6} \text{ sr}^{-1}$ (right). The plots were made with level 3C data files, which only include measurements with $42^\circ < \text{SZA} < 94^\circ$, and QF = 0 or 1.

As expected, cloud frequencies shown in Figure 12 are somewhat higher for the 1G threshold than for the 2G or 5G thresholds. However, false detections will also be higher with the 1G threshold than with higher thresholds. False detection rates are quantified in Figures 13 and 14. Figure 13 shows the total fraction (in percent) of all measurements that were identified as clouds during pre-season and post-season time periods. That is, it shows the total number of clouds divided by the total number of measurements (in percent). We have defined the pre- and post-season time periods to be from 30 to 50 days prior to solstice, and from 70 to 90 days after solstice, respectively. During those time periods no clouds should be detected, so such identifications are false. The analysis reported in Figure 13 is based directly on level 2 (not 3C, as in Figure 12) data, and includes all measurements; no screening has been applied for any reason.

False detection rates are somewhat variable, and are higher in the SH than in the NH (for reasons that are not yet understood). Generally, however, they are less than 2% for the NH and 3% for the SH. These results represent average statistics for all CIPS pixels. However, the false detection rates for the best quality CIPS data ($QF < 2$) are consistently in the 1-2% range whereas the edge pixels ($QF=2$) show consistently higher rates of 2-4% [Lumpe *et al.*, 2013]. This is obviously related to the edge artifacts discussed in relation to the albedo png images above.

The overall picture shown in Figure 13 hides some details of which users should be aware. Figure 14 shows the average

false cloud fraction for the same time periods as in Figure 13, plotted vs. SZA. Calculations of the cloud fractions in Figure 14 identify as "clouds" only those points with albedo $> 10^{-6} \text{ sr}^{-1}$, and omit all data with $QF > 0$. From Figure 14 it is evident that the false cloud detections increase significantly at $SZA < 42^\circ$, which is the reason that the level 2 png files and level 3C files screen out data with $SZA < 42^\circ$.

Figure 14 also shows a peak in false detections at SZA values near 80° . In the SH this peak is particularly noticeable. The CIPS team is still working to understand this increase in false detections, although it is likely related to the fact that the background albedo varies steeply with changing SZA here. The shaded areas in Figures 8 and 9 denote the locations of measurements with $75^\circ < SZA < 85^\circ$ for the orbits shown. On these particular orbits, SZA values in this range are

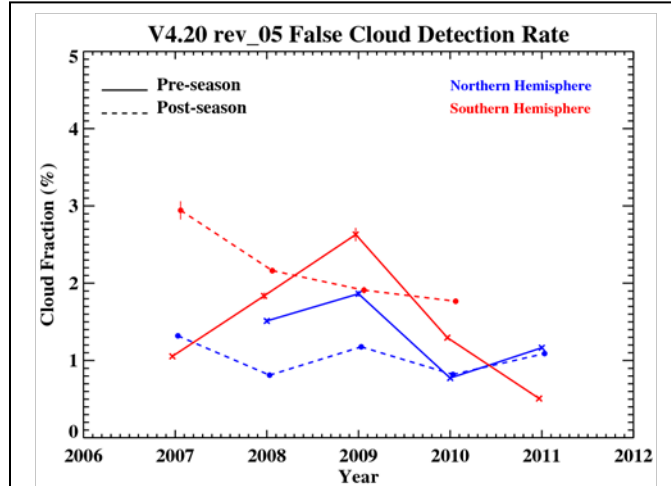


Figure 13. CIPS false cloud detections, plotted as the fraction (%) of measurements during pre-season (50 to 30 days prior to solstice) and post-season (70-90 days after solstice) time periods that were identified as "clouds".

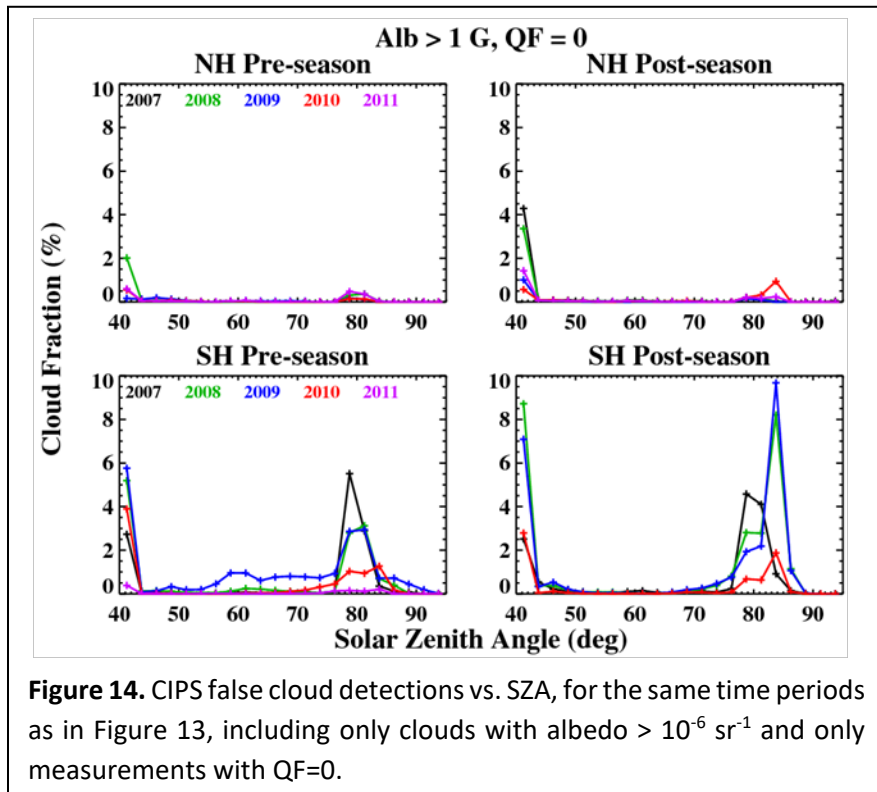


Figure 14. CIPS false cloud detections vs. SZA, for the same time periods as in Figure 13, including only clouds with albedo $> 10^{-6} \text{ sr}^{-1}$ and only measurements with $QF=0$.

found only on the ascending node, near latitudes of 70-80°. When considered over the entire CIPS data set, these SZA values can be found at latitudes as high as the highest latitude extent of the measurements (near 86°). Note that when SZA values in this range correspond to the highest latitudes, they can be found on both the ascending and descending nodes. For albedo $> 2 \times 10^{-6} \text{ sr}^{-1}$ (not shown), the false detections near 80° SZA are generally less than 1%; they range up to ~5% at 40° SZA. Thus, when analyzing data for which the SZA is near 80°, it is prudent to limit the analysis to those measurements for which the albedo is larger than 2G.

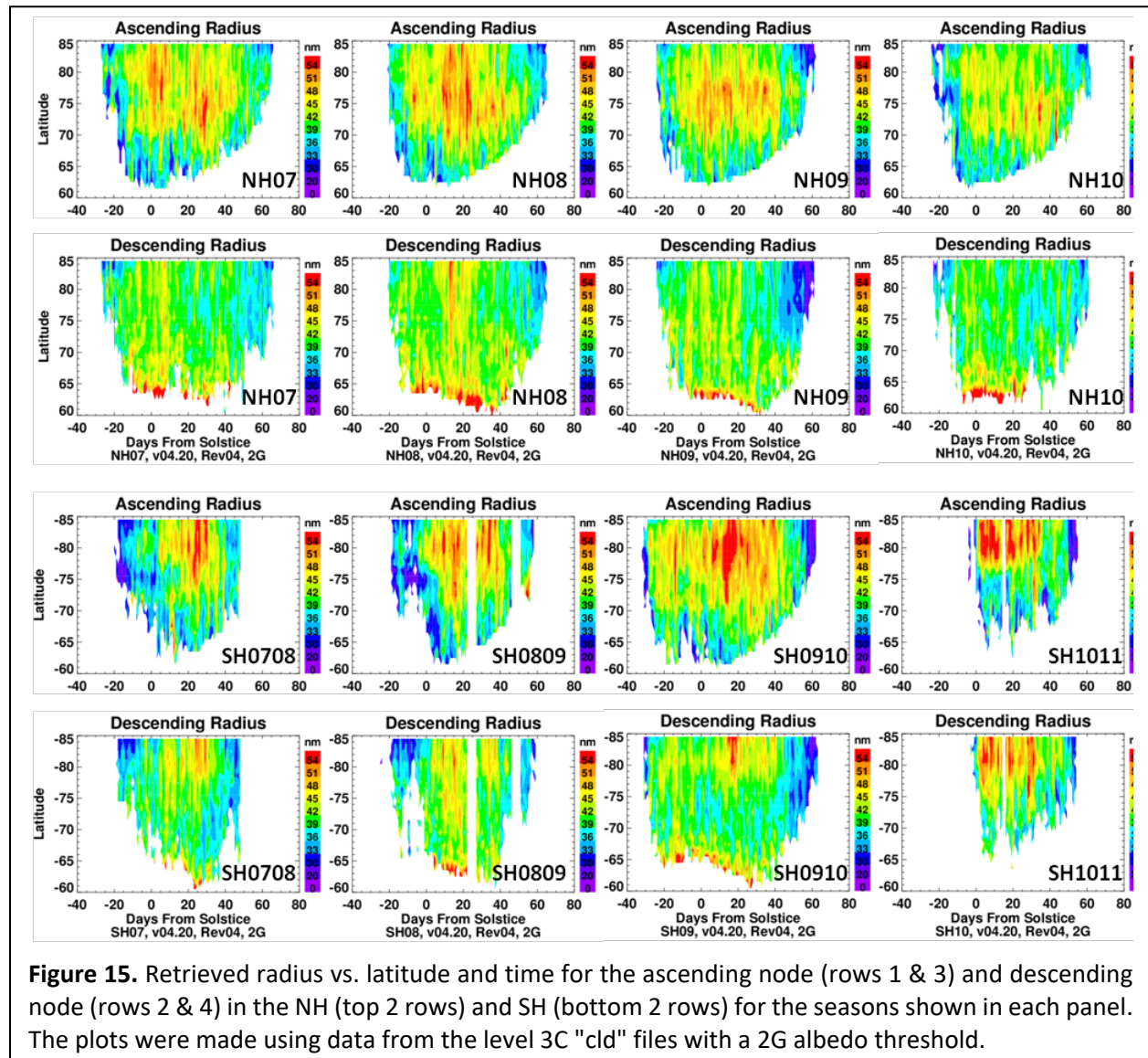
To summarize, CIPS retrieved frequencies are generally valid for scientific analysis for clouds with albedo $> 2 \times 10^{-6} \text{ sr}^{-1}$. They are also valid for clouds with albedos down to $1 \times 10^{-6} \text{ sr}^{-1}$, with the caveat that caution is required at SZA values near 80° and outside the SZA range of 42°-95°. Even for the brighter clouds, though, users should be wary of anomalously high frequencies at these SZA values, since very large false-cloud frequencies are occasionally found on individual, out-of-season orbits in v4.20. In addition, in the NH 2013 season more false detections occurred at SZA $> 92^\circ$ than in previous seasons. We believe this is due to scattered light issues caused by the very large beta angles that AIM began encountering in 2013. Thus users should be cautious of data at SZA $> 92^\circ$ beginning in 2013.

Figure 12 shows that the general morphology for frequency, albedo, and IWC is similar for all thresholds, with largest values at the highest latitudes and in the middle of the season. Note that removal of the dimmest clouds in the 2G and 5G plots results in missing data around the edges of the distributions (early or late in the season, and at the low-latitude edge). The average albedo increases with increasing threshold, since the dimmer clouds are not included in the average for the higher thresholds. Correspondingly, the average IWC also increases. For quantitative interpretations of albedo and IWC, we believe that for most studies valid results will be obtained for clouds brighter than 2G, with $\text{QF} \leq 1$, and with radius $> 20 \text{ nm}$ (see below). If investigating albedo or IWC of clouds for which the albedo ranges from 1-2 G, caution is warranted, but results might still be robust. Retrieved parameters for clouds with albedo $< 1 \text{ G}$ and/or radius $< 20 \text{ nm}$ (see below) are questionable and should not be used.

Figure 12 shows that, unlike the other retrieved cloud parameters, the radius in the NH 2010 season often maximizes near a latitude of about 70-75°. Thus locations with the highest average albedo and occurrence frequency do not correspond to regions with the largest average radius. It is not yet clear if this is a valid result. On the one hand, the morphology for all thresholds is very similar, suggesting that the results even for the 1G threshold are reasonable. On the other hand, however, results for the descending node have a very different morphology. Thus the CIPS team is still evaluating these results, and they are discussed in more detail in the next section.

3.5. Radius Screening

Figure 15 presents contour plots of the retrieved radius vs. time and latitude for all PMC seasons thus far observed by CIPS. The plots in this figure are based on the level 3C "cld" files for the 2G threshold (see the level 3C documentation). Separate plots are shown for the ascending and descending nodes. Although there is substantial variability, in the NH the ascending node radius often maximizes near latitudes of 70°-80°, as was already seen for the NH10 season in Figure 12, rather than at higher latitudes. Similar results are often, although not always, obtained in the SH, although the latitudes of maximum radii are displaced slightly poleward of their location in the NH. In contrast, on the descending node in the NH the radius generally maximizes at the lowest latitudes observed; increases are also seen in the SH descending node data at the lowest latitudes in most seasons, although large radii are found more often (than in the NH) at more polar latitudes as well. In both hemispheres, radii in the middle latitudes of the range shown here are systematically smaller on the descending node than on the ascending node. As shown in the next section, these discrepancies between the ascending and descending node data persist even if a 5G threshold is used. With the higher threshold the lowest latitude clouds are no longer present,



so the increase in radius at the low-latitude edge is either not observed, or is present to only a very limited extent.

That the descending node radius is so large at the lowest latitudes is likely an artifact of the retrievals. Not only is it unexpected from geophysical considerations, but as shown by the fact that these large values mostly disappear when the 5G threshold is used, they overwhelmingly correspond to the dimmest clouds, for which the retrieval uncertainties are largest. That the latitude dependence of the radius is different in the ascending and descending nodes, and that the descending node radii are systematically smaller than the ascending node radii, is currently not understood. It is possible that this is a real effect of diurnal variations (see next section), but caution is warranted before drawing any such conclusion. As discussed in detail in Lumpe et al. [2013] there is a systematic bias in the radius retrievals at low SZA due to the combination of increasing Rayleigh background and decreasing forward-scattering sampling. The retrieved radius is expected to be biased high by up to 10-20 nm for dim clouds ($< 5G$) at SZA less than 55 degrees.

The level 3C files that were used to make the plots in Figure 15 employ a screening such that any cloud with a retrieved mode radius less than 20 nm is removed. Based on radiative transfer principles, CIPS cannot see particles that are only 20 nm in size. It is possible to retrieve such a mode radius because CIPS can see the large-particle end of the size distribution. Since only a small fraction of the particles is observed, however, these determinations have high uncertainty. Thus we recommend that data (including albedo and IWC) for which the retrieved radius is less than 20 nm not be used for scientific analyses at this time.

3.6. Ascending vs. Descending Node Retrievals

In principle, the CIPS data can be used to investigate diurnal variations in PMCs, since ascending node data are acquired at different local times than descending node data. Figure 16 shows the measurement local times for two of the same orbits shown in Figures 8 and 9. The precise range of local times will vary with day of year, but this figure is fairly representative. In the NH, local times on the ascending node range from about 18-24 hours, whereas local times on the descending node range from about 12-18 hours. In the SH, ascending node local times range from about 0 to 6 hours, whereas descending node local time range from about 6-12 hours. At the highest latitudes, the instrument view sweeps quickly through a large range of local times. Because of this, and because these locations see little variation in solar insolation throughout the day, these data are not

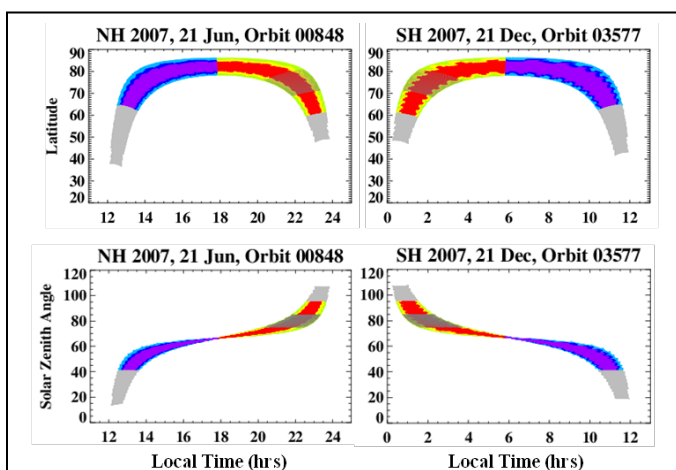


Figure 16. Local time vs. latitude (top) and SZA (bottom) of measurements for orbits 848 in the NH on 21 June 2007 (left) and 3577 in the SH on 21 December 2007 (right). Colors have the same meaning as in Figures 8 and 9.

appropriate for investigations of diurnal variations. Data on the ascending and descending node closer to 65°-70° latitude, however, are separated by around 9-10 hours in local time, and thus in principle contain information about diurnal variations.

As noted above, however, the CIPS retrievals are sensitive to changes in SZA, which by definition are correlated with the local time of the measurements. The bottom panels in Figure 16 show the local time vs. SZA for the same two orbits as the top panels. Recall that CIPS measurements include more forward scattering angles at larger SZA, and that the Rayleigh scattering background is minimized at large SZA, so the uncertainty in the measurements most likely decreases with increasing SZA (until the SZA is so large that the lack of illumination becomes a factor). This suggests that, all other things being equal, the ascending node measurements should have higher accuracy than the descending node measurements. At the current time, there is no theoretical reason to suspect that the higher uncertainties in the descending node should result in a bias (as opposed to simply more "noise" in the retrievals). Nevertheless, we urge caution when interpreting differences between ascending and descending node measurements.

To address this caution in more detail, Figure 17 shows the differences between the ascending and descending node frequencies and particle radii for the NH 2008 season, for the 1G, 2G, and 5G thresholds. Frequencies for the ascending and descending nodes agree within $\pm 8\%$ at all latitudes and times, although there are more areas of small positive differences in the 1G plot than in the 2G or 5G plots. Ascending and descending node radii, on the other hand, show systematic differences at all latitudes other than the very highest; this was also evident in Figure 15. Ascending node radii are larger than

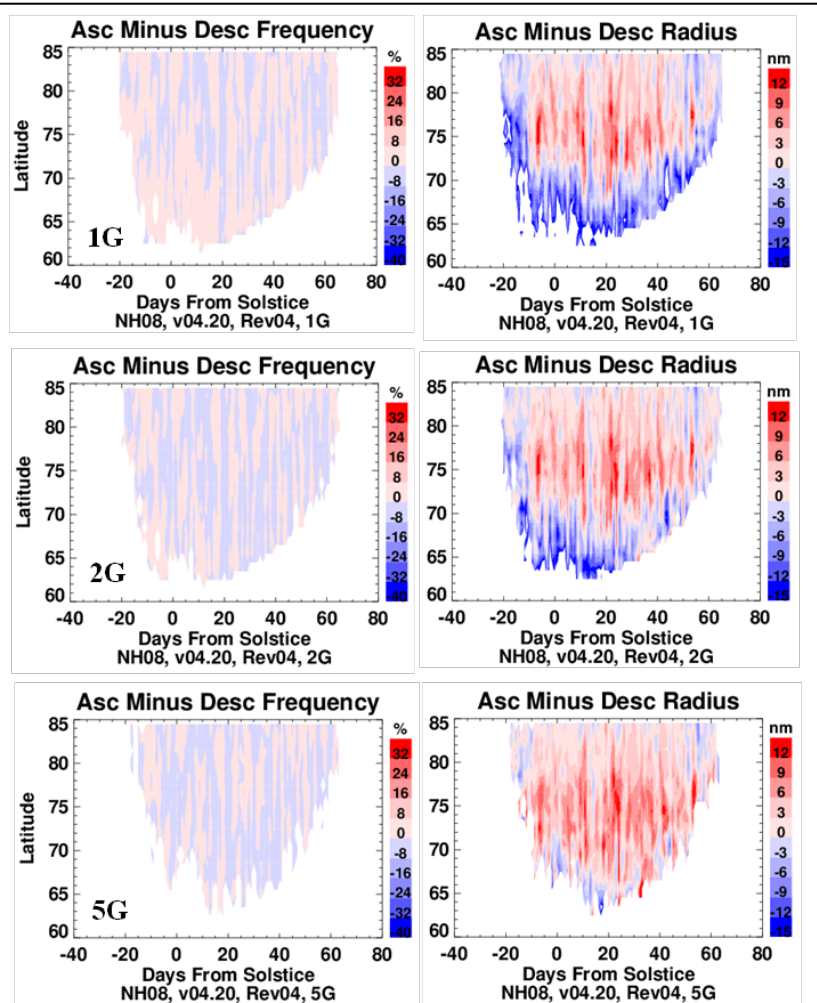


Figure 17. Differences between ascending and descending node PMC frequencies (left) and radius (right) for the NH 2008 season for the 1G threshold (top), 2G threshold (middle) and 5G threshold (bottom).

descending node radii by as much as about 15 nm in the middle of the season for all thresholds. That these differences persist even for the 5G threshold suggests that they are real, but more detailed investigation of the individual retrievals is necessary before this conclusion can be drawn. Ascending node radii are smaller than descending node radii at the lowest latitudes and at the beginning and end of the season; this bias is more pronounced for the 1G threshold, but that is largely because clouds at these times and locations are relatively dim, and are thus removed from the analysis with the higher thresholds.

3.7. Summary

Although the CIPS data are available with minimal screening, we recommend that users apply certain screening themselves when analyzing the data, as summarized here.

Quality Flag: We consider the CIPS data to be robust if the quality flag is 0. Caution is warranted when interpreting albedo values if $QF > 1$. We do not provide radius or IWC values if $QF > 1$.

Solar Zenith Angle: Only data with $42^\circ < SZA < 95^\circ$ are considered robust at this time. In addition, caution is required when interpreting dim clouds near $SZA=80^\circ$, since there are often more false detections near this SZA (for reasons that are not yet understood). Beginning in the NH 2013 season, users will find an increasing number of false detections for $SZA > 92^\circ$.

Albedo Threshold: For qualitative purposes, such as investigations of cloud presence and large-scale patterns, we recommend that only data with albedo larger than 10^{-6} sr^{-1} (1G) be used. For more quantitative analyses of albedo, radius, and IWC, we recommend that only data with albedo larger than 2G be used, although it is possible that albedo values themselves from 1-2 G are valid. Retrieved parameters for clouds with albedo $< 1\text{G}$ should not be used.

Radius: Only data with radius $> 20 \text{ nm}$ should be used for scientific analyses. In addition, caution is warranted when interpreting differences between ascending and descending node radii, as we do not yet know if the differences are valid.

Ascending Node vs. Descending Node: The range of SZA is different in the ascending vs. descending node data. Since the CIPS retrievals are sensitive to SZA, caution is warranted when interpreting ascending vs. descending node differences in all parameters, and especially radii. We recommend that users contact the CIPS team if interested in quantifying diurnal variations.

Finally, a note about the file name convention: Each file has a day-of-year included in the file name. This is the day corresponding to the ascending node equator crossing time. When the equator crossing time is near midnight UT, some or all of the data in the file occur on the day after the day in the filename.

Table 1. Variables in the CIPS level 2 geolocation file. Fill value is NaN.

Note added 22 July 2014: This table was updated to correct errors in the descriptions of UT_Date, UT_Time, and Orbit_Start_Time_UT. Users should be aware that in some of the data files, there is an error in the parameter Orbit_Start_Time_UT. When the error occurs, the symptom is that the yyyymmdd part of Orbit_Start_Time_UT refers to the day the orbit strip finished, rather than the day it started. The error only occurs when the orbit crosses midnight UT, and only on some of these orbits. Whether the error occurs depends on the time between the midnight crossing and start of data collection, so it occurs much more often in the SH than in the NH. This error will be corrected the next time the data are reprocessed. But until then, users may refer to the CIPS website for ascii files that list the affected orbits. No PMC data are affected by this error; it is only in the Orbit_Start_Time_UT variable.

Variable Name	Units	Type/Dimension	Description / Example*
AIM_Orbit_Number		Integer / 1	Integer orbit number to which all data in the file applies / 17365
Version		String / 1	Data version number / 4.20
Revision		String / 1	Data revision number / 05
Product_Creation_Time		String / 1	String containing UT time at which data file was produced / Tue Oct 25 16:31:17 2011
Dependent_1B_Version		String / 1	Version of lower level 1B data used to produce this data set / 04.20
UT_Date		Long / 1	UT date in yyyymmdd format / 20100703
UT_Time	hours	Float / [xdim,ydim]	UT time for each element (fractional hour) / [1933,412], range: 10.3413-10.6638
Hemisphere		String / 1	N (north) or S (south)
Orbit_Start_Time	microseconds	Double / 1	GPS start time of orbit (microseconds from 0000 UT on 6 Jan 1980) / 9.6218671e+014
Orbit_Start_Time_UT	seconds	String / 1	Start time of orbit in yyyymmdd-hr:min:sec format / '20100703-10:04:56'
Orbit_End_Time	microseconds	Double / 1	GPS end time of orbit (microseconds from 0000 UT on 6 Jan 1980) / 9.6219250e+014
Stack_ID		Integer / 1	Obsolete.
XDim		Long / 1	Number of along-orbit-track elements in the data arrays / 1933
YDim		Long / 1	Number of cross-orbit-track elements in the data arrays / 412
NLayers		Integer / [xdim,ydim]	Number of observations at the location of each element; each observation corresponds to a different observing geometry and thus scattering angle in the phase function / [1933,412], range: 1 to 10.

Ratall		Float / [xdim,ydim]	Indicator of forward vs. backward scattering ratio [see Bailey et al., 2009] / [1933,412], range: 0 to 1.28827
Quality_Flags		Float / [xdim,ydim]	Indicators of data quality for each element. In v4.20 the QF is determined only by NLayers as follows: NLayers > 5, QF=0. NLayers = 4 or 5, QF=1. NLayers < 4, QF=2.
KM_Per_Pixel	km	Float / 1	Linear dimension of square pixel occupying area of CIPS resolution element.
BBox	Index	Long / [4]	Bounding Box: Bottom-Left and Top-Right indices of the smallest rectangle which both circumscribes a set of cells on a grid and is parallel to the grid axes / [410, 1187, 2342, 1598]
Center_Lon	Degrees	Double / 1	Center longitude of the orbit / -69.760521
Latitude	Degrees	Float / [xdim,ydim]	Latitude of each element; Latitudes greater (less) than 90 (-90) indicate ascending node data. / [1933,412], range: 38.8969 to 129.829.
Longitude	Degrees	Float / [xdim,ydim]	Longitude of each element; ranges from -180 to 180 / [1933,412], range: -179.999 to 180.000
Zenith_Angle_Ray_Peak	Degrees	Float / [xdim,ydim]	Solar zenith angle (SZA) of each element. The value is specified at the altitude of the maximum contribution to the Rayleigh background. Generally around 55 km but increasing with increasing SZA. / [1933,412], range: 17.2 to 105.5
Common_Volume_Map		Byte / [xdim,ydim]	Indicator for whether this location is within the single "Common Volume" where both CIPS and SOFIE observe each orbit. Indicator 1 = in the common volume; 0 = not in the common volume. / [1933,412], range: 0 to 0.
Notes		String	Any additional notes. / Blank.

* Examples are from cips_sci_2_orbit_17365_2010-184_v04.20_r05_cat.nc.

Table 2. Variables in the CIPS level 2 cloud parameters file. Fill value is NaN.

Variable Name	Units	Type/Dimension	Description / Example*
Percent_Clouds	Percent	Float / 1	Ratio ($\times 100$) of the # clouds detected (cloud_presence_map = 1) to the # locations where it was possible to detect a cloud (cld_albedo ≥ 1). / 53.1911
Cloud_Presence_Map		Float / [xdim,ydim]	Indicator for whether a cloud was detected (1) or not (0). / [1933,412], range: 0 to 1.
Cld_Albedo	10^{-6} sr^{-1}	Float / [xdim,ydim]	Retrieved PMC albedo, defined as the albedo that would be viewed at 90° scattering angle and 0° view angle. Zero implies no cloud was detected at this location. / [1933,412], range: 0.00 to 65.9739.
Cld_Albedo_Unc		Float / [xdim,ydim]	Cloud albedo uncertainty. Not yet populated. Caution is warranted if $QF > 1$.
Particle_Radius	nm	Float / [xdim,ydim]	Retrieved particle mode radius, defined as the mean radius for a Gaussian distribution of particles with an axial ratio of 2 and a distribution width that varies as $0.5 \times \text{radius}$. Zero means no cloud was detected. A value of -999 is reported if $QF > 1$. / [1933,412], range: -999, 0 to 100, in steps of 1.0 nm.
Particle_Radius_Unc		Float / [xdim,ydim]	Particle radius uncertainty. Currently populated with -999 or NaN. Particular caution should be used if the particle radius is less than 20 nm.
Ice_Water_Content	$\mu\text{g m}^{-2}$	Float / [xdim,ydim]	Ice water content at each observation location. Zero means no cloud was detected. A value of -999 is reported if $QF > 1$. / [1933,412], range: -999, 0 to 1.2×10^5 (0.06 to 323 for particle radius > 20 nm).
Ice_Water_Content_Unc		Float / [xdim,ydim]	Ice Water Content uncertainty. Currently populated with -999 or NaN. Particular caution should be used if the particle radius is less than 20 nm.

Ice_Column_Density	ice particles cm ⁻²	Float / [xdim,ydim]	Ice Column Density. Zero means no cloud was detected. A value of -999 is reported if QF>1. / [1933,412], range: -999, 0, 1486.82 to 4.06×10 ¹⁴ (1486.82 to 5.59×10 ⁸ for particle radius > 20 nm).
Chi_Sq		Float / [xdim,ydim]	Chi-squared metric from the fit to the ice phase function used to derive particle properties. This quantity is included for completeness – we make no recommendations for its use in CIPS data analysis. A value of -999 is reported if QF>1. / [1933,412], range: -999, 0 to 21288.

* Examples are from cips_sci_2_orbit_17365_2010-184_v04.20_r05_cld.nc.

Table 3. Variables in the CIPS level 2 phase function file. Fill value is NaN.

Variable Name	Units	Type/Dimension	Description / Example*
Cld_Phase_Albedo	10 ⁻⁶ sr ⁻¹	Float / [xdim,ydim,nlayers]	Cloud scattering phase function - albedo vs. scattering angle. The number of data points in each pixel is given by the Nlayers array (see Table 1; holds for all arrays in this file). / [1933,412,10], range: -516.36 to 601.72.
Cld_Phase_Albedo_Unc	10 ⁻⁶ sr ⁻¹	Float / [xdim,ydim,nlayers]	Uncertainty in cloud phase function. Not yet populated.
Scattering_Angle	Degrees	Float / [xdim,ydim,nlayers]	Scattering angle for each measured data point. / [1933,412,10], range: 16.34 to 179.24.
View_Angle_Ray_Peak	Degrees	Float / [xdim,ydim,nlayers]	Satellite view angle for each measured data point. / [1933,412,10], range: 0.56 to 72.90.

* Examples are from cips_sci_2_orbit_17365_2010-184_v04.20_r05_psf.nc.

References

Bailey, S.M., et al., Phase functions of polar mesospheric cloud ice as observed by the CIPS instrument on the AIM satellite, JASTP 71, 373-380, doi:10.1016/j.jastp.2008.09.039, 2009.

Baumgarten, G., A. Chandran, J. Fiedler, P. Hoffman, N. Kaifler, J. Lumpe, A. Merkel, C. E. Randall, D. Rusch, and G. Thomas, On the horizontal and temporal structure of noctilucent

clouds as observed by satellite and lidar at ALOMAR (69N), *Geophys. Res. Lett.*, 39, L01803, doi:10.1029/2011GL049935, 2012.

Baumgarten, G., J. Fiedler, and M. Rapp, On microphysical processes of noctilucent clouds (NLC): observations and modeling of mean and width of the particle size distribution, *Atmos. Chem. Phys.* 10, 6661-6668, doi:10.5194/acp-10-6661-2010, 2010.

Benze, S., et al., Comparison of polar mesospheric cloud measurements from the Cloud Imaging and Particle Size experiment and the solar backscatter ultraviolet instrument in 2007, *JASTP* 71, 365-372, doi:10.1016/j.jastp.2008.07.014, 2009.

Benze, S., et al., Evaluation of AIM CIPS measurements of Polar Mesospheric Clouds by comparison with SBUV data. *Journal of Atmospheric and Solar-Terrestrial Physics*, doi:10.1016/j.jastp.2011.02.003, 2011.

Chandran, A., D.W. Rusch, G.E. Thomas, S.E. Palo, G. Baumgarten, E.J. Jensen, and A.W. Merkel, Atmospheric gravity wave effects on polar mesospheric clouds: A comparison of numerical simulations from CARMA 2D with AIM observations, *J. Geophys. Res.*, doi:10/1029/2012JD017794, 2012.

Chandran, A., D. W. Rusch, A. W. Merkel, S. E. Palo, G. E. Thomas, M. J. Taylor, S. M. Bailey, and J. M. Russell III, Polar Mesospheric Cloud structures observed from the CIPS experiment on the AIM spacecraft: Atmospheric gravity waves as drivers for longitudinal variability in PMC occurrence, *J. Geophys. Res.*, doi:10.1029/2009JD013185, 2010.

Chandran, A., D. W. Rusch, S. E. Palo, G. E. Thomas, and M. Taylor, Gravity wave observation from the Cloud Imaging and Particle Size (CIPS) Experiment on the AIM Spacecraft, *J. Atmos. Solar-Terr. Phys.*, doi:10.1016/j.jastp.2008.09.041, 2009.

Hervig, M.E., et al., Interpretation of SOFIE PMC measurements: Cloud identification and derivation of mass density, particle shape, and particle size, *JASTP* 71, 316-330, doi:10.1016/j.jastp.2008.07.009, 2009.

Karlsson, B. M., C. E. Randall, T. G. Shepherd, V. L. L. Harvey, J. D. Lumpe, K. Nielsen, S. M. Bailey, M. E. Hervig, and J. M. Russell III, On the seasonal onset of polar mesospheric clouds and the breakdown of the stratospheric polar vortex in the southern hemisphere (2011), *J. Geophys. Res.*, 116, D18107, doi:10.1029/2011JD015989, 2011.

Karlsson, B., C.E. Randall, S. Benze, M. Mills, V.L. Harvey, S.M. Bailey, J.M. Russell III, Intra-seasonal variability of polar mesospheric clouds due to inter-hemispheric coupling, *Geophys. Res. Lett.*, VOL. 36, L20802, doi:10.1029/2009GL040348, 2009.

Lumpe, J. D., S.M. Bailey, J.N. Carstens, C.E. Randall, D. Rusch, G.E. Thomas, K. Nielsen, C. Jeppesen, W.E. McClintock, A.W. Merkel, L. Riesberg, B. Templeman, G. Baumgarten, and J.M.

Russell, III, Retrieval of polar mesospheric cloud properties from CIPS: algorithm description, error analysis and cloud detection sensitivity, *J. Atmos. Solar-Terr. Phys.*, <http://dx.doi.org/10.1016/j.jastp.2013.06.007>, 2013.

Merkel, A. W., D. W. Rusch, S. E. Palo, J. M. Russell III, and S. M. Bailey, Mesospheric planetary wave activity inferred from AIM-CIPS and TIMED-SABER for the northern summer 2007 PMC season. *J. Atmos. Solar-Terr. Phys.*, doi:10.1016/j.jastp.2006.05.01, 2009.

Stevens, M. H., S. Lossow, J. Fiedler, G. Baumgarten, F.J. Lübken, K. Hallgren, P. Hartogh, C.E. Randall, J. Lumpe, S.M. Bailey, R. Niciejewski, R.R. Meier, J.M.C. Plane, A.J. Kochenash, D.P. Murtagh, C.R. Englert, Bright polar mesospheric clouds formed by main engine exhaust from the space shuttle's final launch, *J. Geophys. Res.*, 117, D19206, doi:10.1029/2012JD017638, 2012.

Stevens, M. H., D. E. Siskind, S. D. Eckermann, L. Coy, J. P. McCormack, C. R. Englert, K. W. Hoppel, K. Nielsen, A. J. Kochenash, M. E. Hervig, C. E. Randall, J. Lumpe, S. M. Bailey, M. Rapp & P. Hoffmann, Tidally induced variations of polar mesospheric cloud altitudes and ice water content using a data assimilation system, *J. Geophys. Res.*, 115, D18209, doi:10.1029/2009D013225, 2010.

Created by Cora Randall, Jerry Lumpe, and Brentha Thurairajah, July 2011.